Loss of ellipticity and structural transformations in planar simple crystal lattices

E. A. Podolskaya, A. Yu. Panchenko, A. B. Freidin & A. M. Krivtsov

Acta Mechanica

ISSN 0001-5970
Volume 227
Number 1

Acta Mech (2016) 227:185-201
DOI 10.1007/s00707-015-1424-1

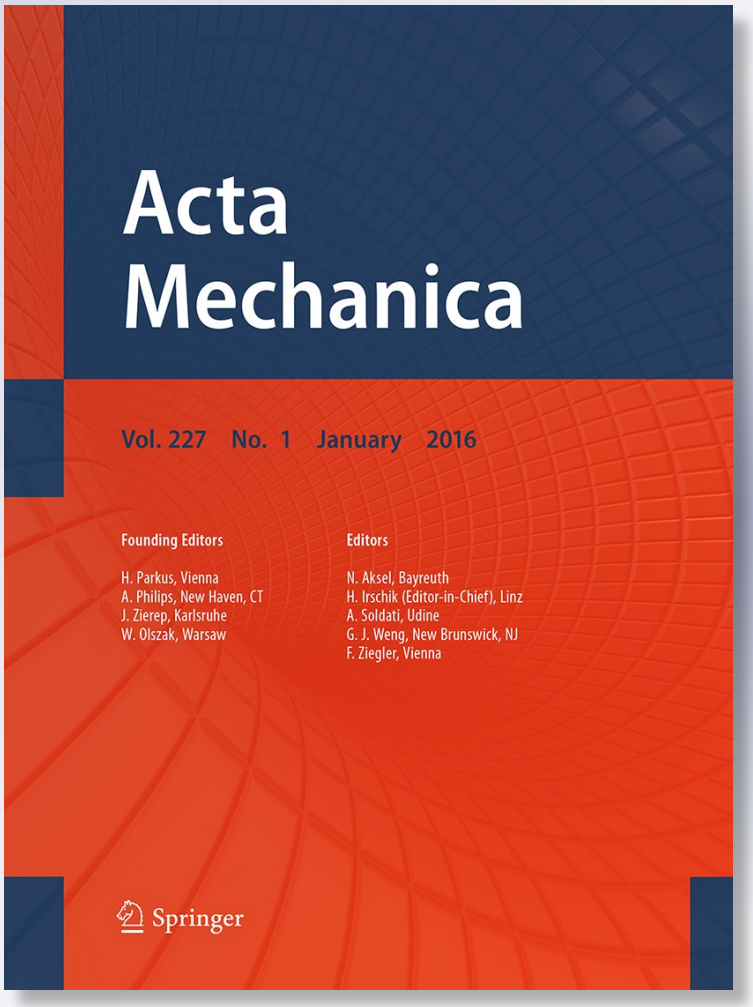

Springer

Acta Mech 227, 185–201 (2016)
DOI 10.1007/s00707-015-1424-1

ORIGINAL PAPER

E. A. Podolskaya · A. Yu. Panchenko · A. B. Freidin · A. M. Krivtsov

Loss of ellipticity and structural transformations in planar simple crystal lattices

Received: 7 November 2014 / Revised: 20 February 2015 / Published online: 7 August 2015

Abstract This work focuses on investigation of structural (phase) transformations in crystal lattices from continuum and discrete points of view. Namely, the continuum, which is equivalent to a simple lattice in the sense of the Cauchy–Born energy, is constructed using long-wave approximation, and its strong ellipticity domains in finite strain space are obtained. It is shown that various domains correspond to variants of triangular and square lattices, and the number of the domains depends on the interaction potential parameters. Non-convex energy profiles and stress–strain diagrams, which are typical for materials allowing twinning and phase transformations, are obtained on the straining paths which connect the domains and cross non-ellipticity zones. The procedures of the lattice stability examinations and estimation of energy relaxation by means of molecular dynamical (MD) simulation are developed, and experimental construction of the envelope of the energy profiles, corresponding to the energy minimizer, is done on several straining paths. The MD experiment also allows to observe the energy minimizing microstructures, such as twins and two-phase structures.

Mathematics Subject Classification 74B20 · 74N05 · 74N15 · 74A50

1 Introduction

One of the motivations for this work is to bridge the gap between continuum and discrete mechanics of structural (phase) transformations. The interfaces which appear due to martensite phase transformations and twinning in deformable solids can be viewed as the surfaces across which the displacement and traction are continuous but some components of the deformation gradient are discontinuous. In contrast to the deformations in a joint body or composite materials where the interfaces between two materials are prescribed by contact surfaces, the interfaces are unknown surfaces. The thermodynamic equilibrium interfaces have to satisfy an additional jump condition, i.e., the continuity of the normal component of the Eshelby stress tensor (see, e.g., monographs [1,2] and reference therein), and in the case of twinning strains are fitted at the interface so that the thermodynamic condition is satisfied automatically [3].

Mathematical modeling of phase transformations starts from the choice of the strain energy function so that the theory can predict what will happen with a given material in various loading conditions. The choice of

E. A. Podolskaya (✉) · A. Yu. Panchenko · A. B. Freidin · A. M. Krivtsov
Institute for Problems in Mechanical Engineering RAS, 61, Bolshoy pr. V. O., St. Petersburg 199178, Russia
E-mail: katepodolskaya@gmail.com

E. A. Podolskaya · A. Yu. Panchenko · A. B. Freidin · A. M. Krivtsov
St. Petersburg Polytechnic University, 29, Politechnicheskaya str., St. Petersburg 195251, Russia

A. B. Freidin
St. Petersburg State University, 28, Universitetsky pr., Peterhof, St. Petersburg 198504, Russia

the strain energy function is usually guided by the results obtained from a number of simple experiments. The problem is that the constitutive equations allow the appearance of strain discontinuity surfaces in an elastic solid only if the strong ellipticity of a material is lost at some deformations [4]. This in turn results in waning parts in stress–strain diagrams and non-convexities of the strain energy which cannot be observed in any experiments because of stability reasons: uniform deformation of a material is not stable at the deformations at which the ellipticity is lost. That is why for a long time the strong ellipticity requirements have been considered as restrictions for the choice of constitutive equations in the sense that "a good material is an elliptic one." But then it became clear that the loss of the strong ellipticity at a certain uniform deformation means that there may exist a non-uniform deformation which is characterized by lower energy (see, e.g., [5,6]). Two-phase deformation is such a non-uniform deformation, and two-phase microstructure growth becomes a mechanism of the energy relaxation. Moreover, on a given straining path, two-phase deformations may be more preferable than uniform one-phase states before the non-ellipticity zone is reached (see, e.g., [7–10]). Thus, on the one hand, non-elliptic branches of the energy dependencies are necessary for phase transitions modeling, and on the other hand, they cannot be obtained from experiments with real materials.

Recently, interest in the discrete and continuum models of crystalline solids has emerged, in particular in connection with stability definition and investigation (see, e.g., [11–13] and reference therein). For example, in [12] it is shown that for Bravais lattices, the discrete and continuum stability regions converge with the increase in the number of particles in a periodic cell, and the stability is defined in terms of energy minimization; this fact is also analyzed numerically in [13]. In the present paper, we restrict ourselves to strong ellipticity analysis for the continuum model and numerical experiments with application to twinning and phase transformations.

We start at microscopic level considering a simple lattice in Sect. 2. Long-wave approximation [14] is used to construct equivalent continuum, and the strong ellipticity conditions are derived for this continuum. Then in Sect. 3 we focus on a planar triangular lattice described by the Morse interaction potential and construct the strong ellipticity region in the strain space. Note that the instability of a planar lattice within the 3D problem statement may lead to the appearance of non-planar configurations (see, e.g., [15,16]). In the present paper, we restrict ourselves to the purely plane case for simplicity of visualization and interpretation, bearing in mind further consideration of 3D lattices in 3D space. The strong ellipticity region, obtained in Sect. 3, consists of a number of domains divided by non-ellipticity zones. We show that these domains can be treated as the domains of strains at which the triangular and square lattice variants can exist. We examine how the energy changes and what are stress–strain diagrams on the straining paths connecting different domains; namely, we obtain non-convex energy profiles and van der Waals type stress–strain diagrams, typical for materials undergoing twinning and phase transformations.

Then in Sect. 4 we return to the discrete lattice. Using MD experiments, we study the lattice behavior on various straining paths. We develop a procedure of "homogeneous" and "inhomogeneous" perturbations to find external strains at which two-phase or twinned microstructures can appear and obtain "real" energy profiles and stress–strain diagrams. We see that experimental dependencies coincide with theoretical ones until the structural transformation starts inside the strong ellipticity domains, and the relaxed energy curve becomes the envelope of the non-convex theoretical curve after new phase domains or twins nucleation. The stress–strain dependence in the case of twinning satisfies the Maxwell equal area rule. Finally we represent and describe the microstructures appeared which minimize the energy. In the Appendix we show the derivation of the formulae for stress tensors, equilibrium and strong ellipticity conditions used in the paper.

2 Strong ellipticity of simple lattices

Let us first describe the material behavior on microscopic level, introducing the common model of the material with microstructure—simple crystal lattice, i.e., the lattice that coincides with its Bravais lattice. Let us assume that the considered lattice is infinite not to account for boundary and surface effects, which, however, become crucial when nanosized objects are regarded. Thus, we can choose any particle, i.e., any nod of the lattice, as a reference particle. In Fig. 1a, which shows a typical part of triangular lattice as an example of simple lattice, the reference particle's position vector is marked as $\mathbf{r}$. Every neighbor of the reference particle located at the distance a_k along the unit vector $\mathbf{e}_k$ has the position vector $\mathbf{r}_k = \mathbf{r} + \mathbf{a}_k$. Due to the symmetry of simple lattices, it has a pair characterized by the same distance $a_{-k} = a_k$ and the unit vector $\mathbf{e}_{-k} = -\mathbf{e}_k$ (see Fig. 1a). The set of particles located at the same distance from the reference particle is called a coordinational sphere. The maximum number of particles in the first coordinational sphere is six for a two-dimensional lattice and twelve for a three-dimensional lattice. The only 2D lattice with six nearest neighbors is the triangular lattice; the

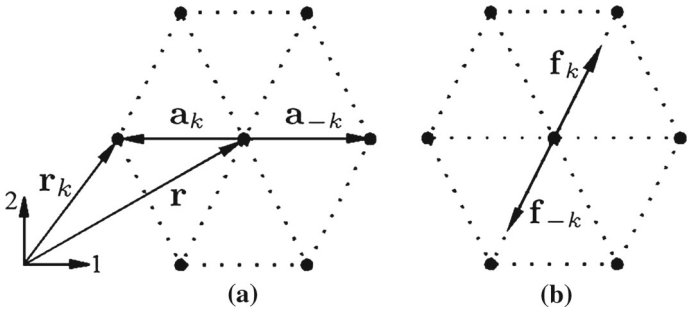

Fig. 1 Simple lattice geometry (**a**) and pair force interaction hypothesis (**b**)

most common 3D lattices with twelve nearest neighbors are encountered in face-centered cubic and hexagonal close-packed structures. In this paper, in Sects. 3 and 4 we will limit ourselves to a triangular lattice as the example of media with microstructure.

In order to describe the geometry in the current configuration, we assume, following Born [14], that the imposed uniform deformation results in a homogeneous displacement field at each representative volume element (RVE). Using the Cauchy–Born rule, we introduce

$$a_k \mathbf{e}_k = \mathsf{F} \cdot a_k^0 \mathbf{e}_k^0, \quad \mathsf{F} = \left(\overset{\circ}{\nabla} \mathbf{r}\right)^{\mathrm{T}}, \qquad \nexists, \tag{1}$$

where a_k^0 and $\mathbf{e}_k^0$ are the reference bond lengths and directions, respectively, a_k and $\mathbf{e}_k$ are the current bond lengths and directions, F is the deformation gradient for the equivalent continuum, the $\circ$ sign above ∇ indicates that the derivatives are calculated with respect to reference configuration, namely

$$\overset{\circ}{\nabla} \mathbf{r} \equiv \sum_n \mathbf{i}_n \frac{\partial \mathbf{r}}{\partial r_n^0},$$

where r_n^0 are Lagrangian coordinates in the orthonormal basis $\mathbf{i}_n$. The absence of higher degrees of deformation gradient is the result of the long-wave approximation. This rule is valid for simple lattices and has to be modified for complex lattices (see, e.g., [17]).

The interaction law at microscopic level is introduced by means of interaction potentials. In this paper, we use the pair force interaction: particles are connected with other particles by nonlinear springs, and the potential Π depends on relative displacements only. Let us denote $\Pi_k = \Pi(a_k)$ and introduce the interaction force $\mathbf{f}_k = \Pi_k' \mathbf{e}_k = \Pi'(a_k)\,\mathbf{e}_k$ (see Fig. 1b) and bond stiffness $\Pi_k'' = \Pi''(a_k)$. The most common interaction laws provide repulsion upon compression, cohesion upon stretching and only one equilibrium bond distance (the distance at which two particles are at equilibrium), i.e., the solution of $\Pi'(r) = 0$ is unique; also $\Pi(r) \to 0$ when $r \to \infty$.

To build the bridge between continuum and discrete representation of the material, the Cauchy–Born energy is used as the energy of the equivalent continuum in the absence of body forces [11,18]

$$W = \frac{1}{2V_0} \sum_k \Pi_k, \tag{2}$$

where V_0 is the unit cell (RVE) volume in the reference configuration, and the energy is summed over all considered coordinational spheres. In the case of pair force interaction, potentials Π_k depend on relative displacements only, which in turn can be expressed in terms of the deformation gradient F using (1). Then the Piola stress tensor for equivalent continuum can be calculated as (see the Appendix)

$$\mathsf{P} \equiv \frac{\partial W}{\partial \mathsf{F}^{\mathrm{T}}} = \frac{1}{2V_0} \sum_k \Pi_k' a_k^0 \mathbf{e}_k^0 \mathbf{e}_k, \tag{3}$$

and the Cauchy stress tensor is

$$\sigma = \frac{1}{2V} \sum_k \Pi'_k a_k \mathbf{e}_k \mathbf{e}_k, \tag{4}$$

where V is the unit cell (RVE) volume in the current configuration, and the condition $\sigma = 0$ determines the distances between the particles at microscopic level which correspond to the stress-free state of the lattice. Due to the symmetry of simple lattices, the tensor equation $\sigma = 0$ yields only one scalar equation, which has the unique solution under the aforementioned assumptions on the interaction potential. The solution has a smaller value than the equilibrium bond distance, if more than one coordinational sphere is regarded, and is exactly equal to it for nearest neighbor interaction.

The symmetry of the simple lattice under pair force interaction assumption ensures its equilibrium at arbitrary uniform strain at both micro- (see Fig. 1b) and macroscopic levels, because within long-wave approximation (see the Appendix)

$$\sum_k (\mathbf{f}_k + \mathbf{f}_{-k}) = 0 \;\Leftrightarrow\; \overset{\circ}{\nabla} \cdot \mathsf{P} = 0.$$

As the equilibrium equations hold identically, it is possible to obtain the strong ellipticity condition for equivalent continuum, which is a necessary stability condition for a uniformly deformed material [5]. Let us impose a minor perturbation on the pre-strained lattice at the microscopic level. This leads to the following equation of motion for the equivalent continuum:

$$\rho_0 \delta \ddot{\mathbf{u}} = \delta \left(\overset{\circ}{\nabla} \cdot \mathsf{P} \right), \tag{5}$$

where $\mathbf{u}$ is the displacement field, $\rho_0 = \dfrac{m}{V_0}$ is the density, and m is the total mass of the particles, located in V_0.

Taking into account that $\overset{\circ}{\nabla} = \left(\overset{\circ}{\nabla} \mathbf{r} \right) \cdot \nabla$ and denoting $\mathbf{v} = \delta \mathbf{u}$, we obtain the following wave equation [19] (see the Appendix):

$$\ddot{\mathbf{v}} = {}^4\mathsf{Q} \cdots \nabla \nabla \mathbf{v},$$

where

$$\begin{gathered} {}^4\mathsf{Q} = \left(\mathsf{I}\Phi + {}^4\Psi \right), \qquad \Phi = \frac{1}{2V_0\rho_0} \sum_k \Pi'_k a_k \mathbf{e}_k \mathbf{e}_k, \\ {}^4\Psi = \frac{1}{2V_0\rho_0} \sum_k a_k^2 \left(\Pi''_k - \frac{\Pi'_k}{a_k} \right) \mathbf{e}_k \mathbf{e}_k \mathbf{e}_k \mathbf{e}_k. \end{gathered} \tag{6}$$

Here I is the unit tensor, and the fourth-rank tensor ${}^4\mathsf{Q}$ is expressed in terms of microscopic characteristics, and thus, ${}^4\mathsf{Q}$ depends on the deformation gradient F only. Searching the solution in wave form $\mathbf{v} = \mathbf{v}_0 e^{i\omega t} e^{i\mathbf{k}\cdot\mathbf{r}}$, where $\mathbf{k}$ is the wave vector and ω is the frequency, we get

$$\left(\mathsf{D} - \omega^2 \mathsf{I} \right) \cdot \mathbf{v}_0 = 0, \qquad \mathsf{D} = {}^4\mathsf{Q} \cdot \cdot \mathbf{k}\mathbf{k},$$

and the frequencies of the elastic waves in the equivalent continuum are real if and only if the acoustic tensor D is positive definite. Thus, the strong ellipticity condition for the simple lattice, treated as the equivalent continuum, takes the form of the positive definiteness of the acoustic tensor D expressed by (6) in terms of lattice parameters a_k, $\mathbf{e}_k$, derivatives of the energy (2) and wave vector.

In the next sections, the condition

$$\mathsf{D}(\mathbf{k}) > 0 \quad \forall \mathbf{k} \neq 0 \tag{7}$$

is specified for the planar triangular lattice. This allows us to construct the non-ellipticity domain in strain space. Then structural transformations as the mechanisms of energy relaxation are observed using MD simulation on straining paths which cross the non-ellipticity domain.

3 Strong ellipticity analysis for triangular lattice

3.1 Strong ellipticity domains

A typical part of a triangular lattice is shown in Fig. 1. The uniform deformation gradient F in the 2D case can be represented in the following form using QR decomposition:

$$\mathsf{F} = \hat{\mathsf{Q}} \cdot \hat{\mathsf{F}}.$$

Here $\hat{\mathsf{Q}}$ is an orthogonal tensor, and $\hat{\mathsf{F}}$ has upper triangular matrix form. Taking objectivity considerations into account and also bearing in mind that the lattice is infinite, so that boundaries are not regarded, we will further restrict ourselves to the deformation gradients for which $\hat{\mathsf{Q}}$ is a unit tensor. Thus, F will have the following matrix form:

$$\mathsf{F} \sim \begin{pmatrix} 1+\varepsilon_{11} & \operatorname{tg}\varphi \\ 0 & 1+\varepsilon_{22} \end{pmatrix}, \tag{8}$$

which is an affine transformation with extension in directions 1 and 2, and shearing in the direction 1; indices 1 and 2 correspond to the coordinate axes introduced in Fig. 1, ε_{11} and ε_{22} are strains along the respective axes, and φ is a shear angle.

Substituting the deformation gradient (8) into (1), we calculate current bond lengths and directions, and using (7), we obtain strong ellipticity conditions in the form

$$\begin{aligned} &\operatorname{tr}\mathsf{D} > 0 \Leftrightarrow A_1 k_1^2 + B_1 k_1 k_2 + C_1 k_2^2 > 0, \\ &\det\mathsf{D} > 0 \Leftrightarrow A_2 k_1^4 + B_2 k_1^2 k_2^2 + C_2 k_2^4 + D_2 k_1^3 k_2 + E_2 k_1 k_2^3 > 0, \end{aligned} \tag{9}$$

where k_1 and k_2 are components of the wave vector and the coefficients A_1, B_1, C_1, A_2, B_2, C_2, D_2, E_2 depend on the components of tensor ${}^4\mathsf{Q}$, and, thus, on the strain parameters ε_{11}, ε_{22}, $\operatorname{tg}\varphi$:

$$\begin{gathered} A_1 = Q_{11} + Q_{21}, \quad B_1 = Q_{14} + Q_{24}, \quad C_1 = Q_{12} + Q_{22}, \\ A_2 = Q_{11}Q_{21} - Q_{41}^2, \quad B_2 = Q_{14}Q_{24} + Q_{11}Q_{22} + Q_{12}Q_{21} - 2Q_{41}Q_{42} - Q_{44}^2, \quad C_2 = Q_{12}Q_{22} - Q_{42}^2, \\ D_2 = 2\left(Q_{11}Q_{24} - 2Q_{41}Q_{44} + Q_{14}Q_{21}\right), \quad E_2 = 2\left(Q_{12}Q_{24} - 2Q_{42}Q_{44} + Q_{14}Q_{22}\right). \end{gathered}$$

Here the following notation is used to pass from four indices to two indices due to the symmetry of formula (6): $11 \to 1,\ 22 \to 2,\ 12 = 21 \to 4$.

Further, we take the interaction law in the form of the Morse potential

$$\Pi(r) = D\left[e^{-2\theta\left(\frac{r}{a}-1\right)} - 2e^{-\theta\left(\frac{r}{a}-1\right)}\right]. \tag{10}$$

The parameter D is the depth of the potential well, θ is responsible for the well width, and a is the equilibrium bond distance. For the sake of the result representativeness, we take $\theta = 6$, unless otherwise specified. Note that at this particular θ the Morse potential is equivalent to the Lennard-Jones potential at $r \approx a$ [18].

Figure 2 shows the strong ellipticity region for the planar triangular lattice in strain space ε_{11}, ε_{22}, $\operatorname{tg}\varphi$. We show only the case $\varphi \geq 0$, and the picture is mirrored with respect to the plane ε_{11}, ε_{22} at $\varphi < 0$. In general, one can distinguish between five domains denoted as I, II, III, IV and V. The shape, the size and the number of the domains depend on the interaction potential parameters, and the minor domains III and V vanish as the parameter θ decreases.

Typical lattice states which correspond to different domains are presented in Fig. 3. Here the RVE is gray, the reference particle is in the center of the figures, the nearest neighbors in the reference configuration are black circles of a smaller radius, and the particles of the reference second coordinational sphere are depicted as empty circles. The domain I contains the point $\varepsilon_{11} = \varepsilon_{22} = \operatorname{tg}\varphi = 0$, and the lattices at strains from the domain I can be referred to as the deformed lattice "a." The domain II contains the point $\varepsilon_{11} = \sqrt{3}-1$, $\varepsilon_{22} = 1/\sqrt{3}-1$, $\operatorname{tg}\varphi = 0$ that corresponds to the triangular lattice "b," and lattices at strains from the domain II can be considered as the deformed lattice "b," and, finally, the strains from the domain IV can be considered as the strains of the triangular lattice "c" with the reference state at $\varepsilon_{11} = \varepsilon_{22} = 0$, $\operatorname{tg}\varphi = 2/\sqrt{3}$. Further, we will refer to the lattice states at strains from the domains I, II and IV as to the deformed variants "a," "b" and "c" of the "triangular phase," and it will be shown that the states "a," "b" and "c" of the triangular lattice are stress-free states.

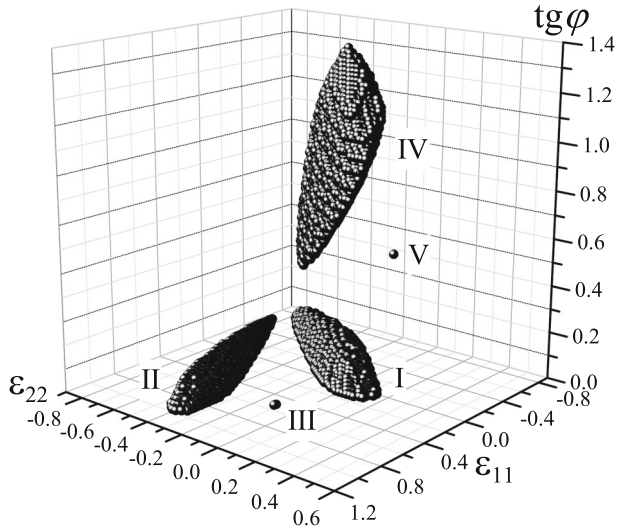

Fig. 2 Strong ellipticity domains for triangular lattice in strain space ε_{11}, ε_{22}, $\mathrm{tg}\,\varphi$. The Morse potential with $\theta = 6$

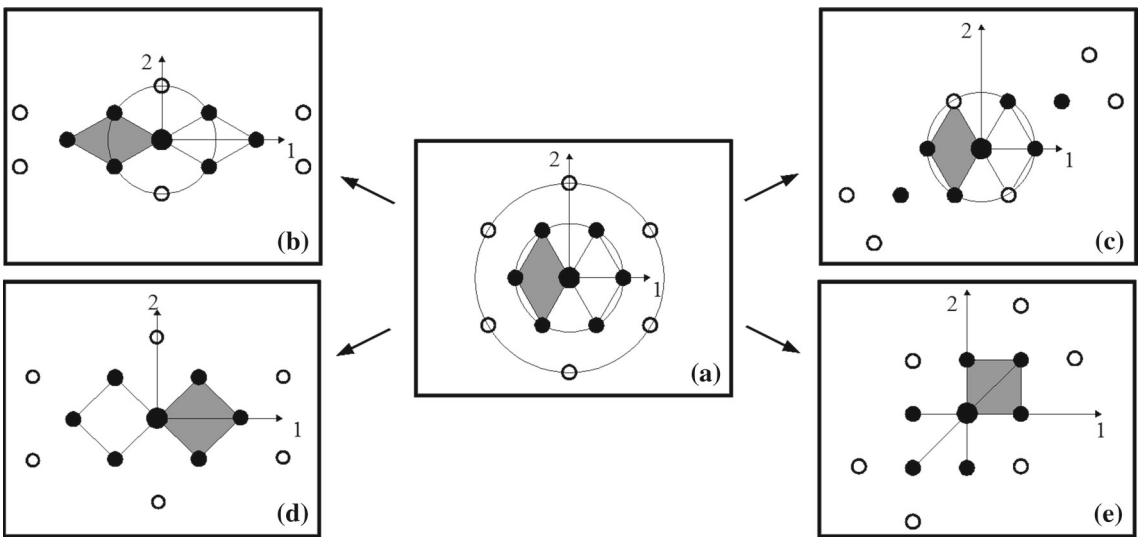

Fig. 3 The states of the triangular lattice typical for the strong ellipticity domains: **a** vertical orientation of RVE (reference configuration, domain I), **b** horizontal orientation of RVE (domain II), **c** vertical orientation of RVE (domain IV), **d**, **e** square RVE (domains III and V)

The lattice configurations at strains from domains III and V can be regarded as deformed square lattices "d" and "e." It is known that the pair force interaction does not allow the stability of stress-free square lattice, because its shear modulus is zero within nearest neighbor interaction [18]. Indeed, in this case, the forces do not produce any work upon shearing due to the symmetry of the lattice. Thus, in contrast to the "triangular phase," the square lattices "d" and "e" can be strongly elliptic only at all-round extension. Further, we will refer to the lattice states at strains from the domains III and V as to states of the "square phase."

The use of the terms from the phase transition theory, namely a distinction between the deformed variants of the triangular phase and deformed states of the square phase, is supported by the fact that the different lattice states take place at strains which correspond to different convex branches of the lattice energy dependencies on strains divided by non-convex curve pieces (see below).

Judging by Fig. 3, one can expect that surfaces of strain discontinuities can appear on the straining paths which connect different ellipticity zones. These surfaces form twins on the paths connecting domains I and II, I and IV, and II and IV with coexisting variants of lattices with different RVE orientations: "a" and "b," "a" and "c," and "b" and "c," respectively, and interphase boundaries on the paths connecting domains I and

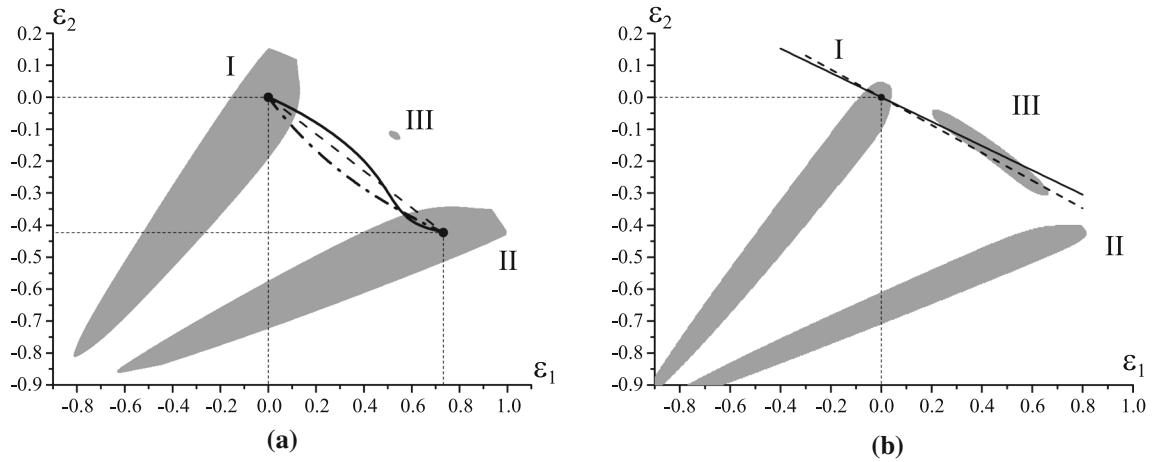

Fig. 4 Strong ellipticity regions' cross section at $\varphi = 0$ for the Morse potential at $\theta = 6$ (**a**) and $\theta = 20$ (**b**)

III, I and V, II and III, etc. which correspond to coexisting triangular and square phases. Note that the phase transformations are possible only at those interaction potential parameters at which the domains III and V exist.

3.2 Biaxial straining paths at $\varphi = 0$

Now we focus on the cross section of the strong ellipticity region by the plane $\varphi = 0$ that contains cross sections of the domains I, II and III (Fig. 4a). In this case, the eigenvectors of deformation gradient and, consequently, of the Cauchy stress tensor coincide with the axes 1 and 2 shown in Fig. 1, $\varepsilon_1 \equiv \varepsilon_{11}$, $\varepsilon_2 \equiv \varepsilon_{22}$. Note that the coordinates $\tilde{\varepsilon}_1, \tilde{\varepsilon}_2$ can be chosen in which the domains I and II in the plane $\varphi = 0$ become symmetric with respect to the line $\tilde{\varepsilon}_1 = \tilde{\varepsilon}_2$. If the origin is placed in stress-free square state, then

$$\tilde{\varepsilon}_1 = \frac{1+\varepsilon_1}{\sqrt{2}} - 1, \qquad \tilde{\varepsilon}_2 = \frac{\sqrt{3}(1+\varepsilon_2)}{\sqrt{2}} - 1.$$

The strong ellipticity domains are determined by the simplified inequalities (9)

$$\begin{aligned} &\operatorname{tr} \mathsf{D} > 0 \Leftrightarrow A_1 k_1^2 + C_1 k_2^2 > 0, \\ &\det \mathsf{D} > 0 \Leftrightarrow A_2 k_1^4 + B_2 k_1^2 k_2^2 + C_2 k_2^4 > 0, \end{aligned} \tag{11}$$

because multipliers like Q_{14} vanish, when off-diagonal components of F are absent. It is possible to exclude the components of $\mathbf{k}$ from (11), so that the strong ellipticity conditions are expressed in terms of the components of tensor ${}^4\mathsf{Q}$ only [19], i.e.,

$$\begin{aligned} &Q_{11} > 0, \quad Q_{21} > 0, \quad Q_{12} > 0, \quad Q_{12} > 0, \quad B_2 > -\sqrt{A_2 C_2}, \\ &A_2 = Q_{11} Q_{21}, \quad C_2 = Q_{12} Q_{22}, \quad 2B_2 = Q_{11} Q_{22} + Q_{12} Q_{21} - 4Q_{44}^2. \end{aligned} \tag{12}$$

Note that on the strong ellipticity domains' boundaries positivity is lost either by one of the instantaneous Young's moduli or by one of the instantaneous shear moduli [19].

Black dots in Fig. 4a correspond to the reference lattice states "a" and "b" in Fig. 3. Three straining paths connecting these states are indicated: the solid curve is the uniaxial loading path along the axis 1, the dash-dotted curve is constant volume curve, and the dashed line is just a straight line.

To confirm that the lattice variant "b" is stress free in its reference state, we construct a stress–strain diagram along the uniaxial loading path. The dependence of σ_1 on ε_1 at $\sigma_2 = 0$ is shown in Fig. 5a where σ_1 and σ_2 are the eigenvalues of the Cauchy stress tensor (4). Strains and corresponding stresses at which the material is strongly elliptic belong to the hatched zones. There are three stress-free states and, evidently, the left one matches the lattice variant "a" and the right one matches "b." The middle one corresponds to the stress-free

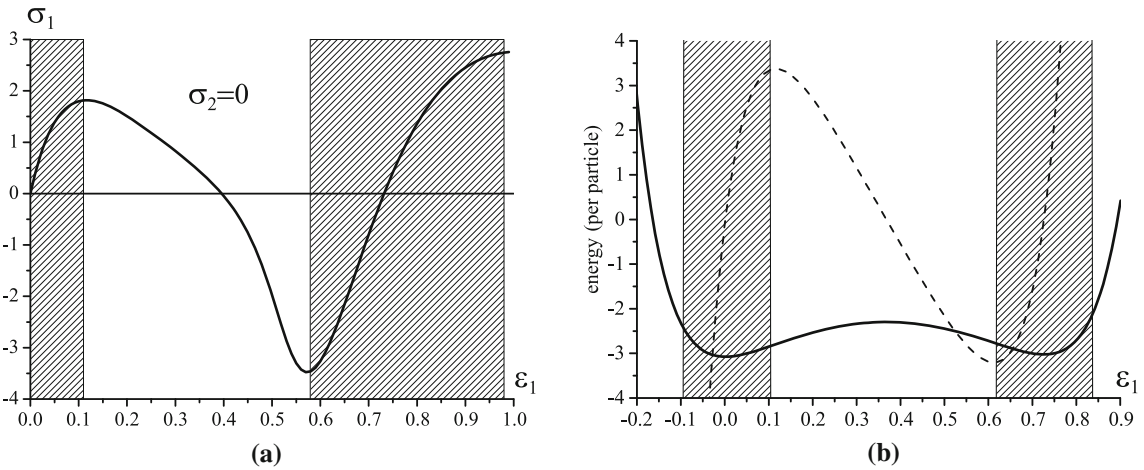

Fig. 5 Transition from triangular phase to triangular phase. **a** Stress–strain diagram at uniaxial loading connecting configurations shown in Fig. 3 "a" and "b" (*solid line* in Fig. 4a), **b** energy (*solid*) and its derivative (*dashed*) on the straight line path connecting configurations shown in Fig. 3 "a" and "b" (*dashed line* in Fig. 4a). Strong ellipticity zones are hatched. The Morse potential, $\theta = 6$

square lattice. One can see that both strong ellipticity domains I and II contain stress-free states of the triangular configurations, but the stress-free square lattice cannot exist in the strong ellipticity domain.

Figure 5b shows the energy (solid line) and its first derivative (dashed line) along the straight line connecting two stress-free states "a" and "b" in Fig. 4a. Two minima are of equal depth, as expected. They are separated by the non-ellipticity zone where the energy is non-convex.

In the next section, using MD simulation we will demonstrate that the boundaries separating the grains occupied by the lattices with various orientations (twins) appear on the straining paths connecting stress-free states. We will show the results only for the path on which the sample's volume is constant (dash-dotted curve in Fig. 4a) in order to focus on shearing deformation mechanisms and get clear picture without additional vacancies, holes and cracks due to volume changes.

To make the transformation from triangular phase to square phase more visible, we enlarge the domain III by changing the potential parameter θ from $\theta = 6$ to $\theta = 20$ (Fig. 4b). This also leads to approaching of the domain III to the point that corresponds to the stress-free square lattice configuration. Besides, the thickness of the domains I and II decreases.

To demonstrate the energy changes due to the lattice evolution if the phase state changes, we consider two straight line straining paths connecting domains I and III. Both lines start from the reference strain of the stress-free lattice variant "a." The stress-free square lattice lies outside the strong ellipticity zone, but close to the intersection of the axis $\tilde{\varepsilon}_1 = \tilde{\varepsilon}_2$ of the square lattice all-round extension and the boundary of domain III. The dashed line passes the stress-free triangular state and this intersection. The solid line just crosses the domain III. The energy changes on two paths are shown in Fig. 6. One can see that two uniformly deformed phases can indeed exist in strong ellipticity zones, but the square phase can exist only in the stressed state, as there is no minimum in the strong ellipticity zone. The non-convexity of the energy profile allows us to expect the appearance of two-phase deformations on these straining paths, and this is confirmed in the next section by MD experiments.

4 MD simulation of structural transformations: relaxed energy

In this section, the evolution of the triangular lattice is investigated by means of MD simulation along particular straining paths mentioned above. The simulation technique in general is described in [18]. In the present paper, we develop the procedures of the lattice stability examinations and estimation of energy relaxation from unstable states. We also observe the appearance of microstructures as the mechanism of the energy relaxation.

The strain space $\varepsilon_1, \varepsilon_2$ is divided into a grid. For each node, we construct a triangular lattice in the corresponding deformed state with periodic boundary conditions so that to bring the system to the state considered theoretically. The interaction between the particles is described by the Morse potential (10).

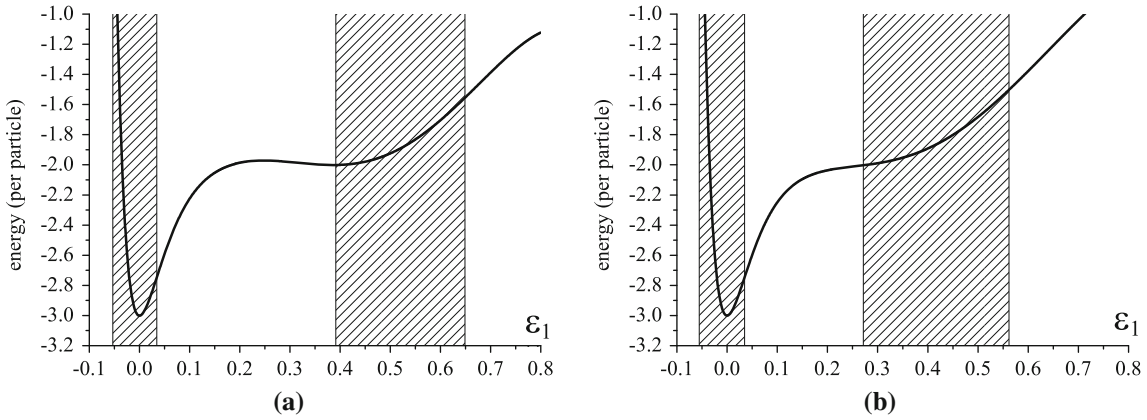

Fig. 6 Transition from triangular phase to square phase. Energy on the paths connecting stress-free configuration "a" and all-round extended configuration "d" (see Fig. 3): **a** on the *dashed line*, **b** on the *solid line* (see Fig. 4b). Strong ellipticity zones are hatched. The Morse potential, $\theta = 20$

Stability examination is carried out using two types of perturbations: "homogeneous" and "inhomogeneous" ones; in both cases, they are caused by introduction of initial kinetic energy. Within the "homogeneous" approach, a small random velocity with normal distribution is attributed to each particle so that the average kinetic energy of the sample is about six orders of magnitude smaller than the depth of the potential well D, i.e., the energy required to evaporate the sample. The system evolution is described by the solution of the Cauchy problem for the set of ordinary differential equations for the particles

$$m\ddot{\mathbf{r}}_k = \sum_{n=1}^{N} f\left(|\mathbf{r}_k - \mathbf{r}_n|\right) \frac{\mathbf{r}_k - \mathbf{r}_n}{|\mathbf{r}_k - \mathbf{r}_n|}, \tag{13}$$

where N is the number of particles, m is the particle mass, and $\mathbf{r}_k$ is the position vector of the kth particle, using the Verlet algorithm [20]. The calculation step is $0.01T$, where T is the period of small oscillations of an isolated pair of particles.

We calculate the kinetic energy per particle. If at a given strain the kinetic energy starts growing and exceeds the initial value, then the configuration is considered as unstable. Since perturbation is caused only by velocities, the kinetic energy E_k partially converts to potential energy right away (less than within $5T$), e.g., for linear systems the value of the average kinetic energy is two times smaller than that of the initial E_k [21]. Thus, the only reason for the kinetic energy to exceed the initial E_k is the decrease in the value of the potential energy, which is associated with structural changes in the material. The number of calculation steps before the instability arises depends on the given strain and varies from tens to hundreds of thousands. In order to speed up the calculations, we use the following scheme. At the first stage, before the onset of instability, the calculation is carried out in accordance with the Verlet list of interactions [20], which are compiled prior to the computation. This approach is justified by the fact that the list of interactions does not change in a stable configuration at low levels of average kinetic energy. At the next stage, if the instability is detected, Verlet lists are recompiled every 20 steps, i.e., $0.2T$, using the cell-linked list method [22]. We wait $500T$ until a new equilibrium microstructure is formed. Our calculations showed that this time is sufficient for the structure to form and for the kinetic energy to change its behavior from growing to oscillating. After that, we slowly "cool" the system introducing a dissipation coefficient which depends on the average kinetic energy and calculate the relaxed energy. We take ν in the form

$$\nu = \nu_0 \left(\nu_A - \frac{\nu_B E_k^2}{E_k^2 + \nu_C} \right), \tag{14}$$

where the parameter $\nu_0 = 2\sqrt{mC}$ is the critical damping coefficient, C is the stiffness of the bond between particles, and $\nu_A = 0.3,\ \nu_B = 0.295,\ \nu_C = 0.01D$ are certain constants chosen in a way as to minimize the cooling time and, at the same time, to ensure sufficient moveability of the particles for prospective structural rearrangement.

When the value of the average kinetic energy per particle becomes smaller than $D \cdot 10^{-3}$, the particles' velocities are decreased by ten times every $50T$, since at this value of the kinetic energy the structure of the material is no longer changing. The cooling process is assumed to be completed with sufficient precision when the value of the average kinetic energy becomes smaller than $D \cdot 10^{-4}$ within $50T$. Note that the dimension of the stability region in strain space depends on the number of the calculation steps; its size decreases and the obtained stability boundary tends to the theoretical strong ellipticity boundary shown in Fig. 4 with increasing number of steps. After the cooling is completed, the average values of the mechanical properties of the material are calculated, and the averaging time is $300T$.

We emphasize that the instability region does not overlay the strong ellipticity region at the homogeneous perturbations considered. But it is known that a phase transformation can start before the local stability of a parent phase is lost. Recall that only purified gas and liquid can be in undercooled or superheated states, respectively, in phase transitions "gas–liquid," and the Maxwell rule allows a phase transformation to start earlier owing to the existence of inhomogenous perturbations.

Having this in mind, we develop the "inhomogeneous" perturbations approach. First, a uniform deformation and a random minor velocity field is imposed on the lattice like in the previous case. Then a zone with the area of about one quarter of the sample's area is chosen in the sample's center. The particles' velocities are additionally increased inside this zone so that the kinetic energy averaged over the zone becomes only one order of magnitude smaller than the depth of the potential well. The instability exhibits as the appearance of the torn bonds and the particles' rearrangements. After that, we wait again until the microstructure is formed, "cool" the system and calculate the relaxed energy. This procedure allows us to obtain the relaxed microstructures with energies which are closest to the minimum possible energy in terms of value, obviously exceeding it due to imperfections. Thus, using two types of perturbations, we obtain experimentally both a lower energy bound and stability bounds. The randomness of the initial velocity distribution accounts for non-uniqueness of the static solution after strong ellipticity loss. The relaxed microstructures vary from one run of the experiment to another, but the main features remain the same.

Figure 7 shows the energy and shear stress dependencies on strain along the constant volume straining path $(1 + \varepsilon_1)\,(1 + \varepsilon_2) = 1$ connecting the stress-free triangular states "a" and "b" in strain space (dash-dotted curve in Fig. 4a). In theoretical analysis that does not account for evolution after strong ellipticity loss, it means that both the sample's and the unit cell's volumes are fixed and equal to the corresponding volumes of the stress-free state, as only uniform deformations are considered. In the MD simulation, we can fix the sample's volume alone, thus allowing for structural transformations, and the unit cell's volume is fixed only as the initial condition for particle positions. Such a straining path enables us to exclude the influence of all-round extension or compression and focus on shearing deformation mechanisms. The dashed line in Fig. 7a shows the energy calculated theoretically for uniformly deformed lattice as it was done in the previous section for the Morse potential with $\theta = 6$. The solid line is obtained by the MD experiment after the energy relaxation. Here the energy jumps are nucleation barriers, and the other part of the curve forms the envelope of the theoretical energy profile obtained for the uniformly deformed lattice.

Experimental (solid line) and theoretical (dashed line) shear stress–shear strain dependencies are shown in Fig. 7b. In the chosen coordinates, the theoretical curve is analogous to the van der Waals isotherm in the pressure–volume diagram for a phase transition "gas–liquid," and the experimental line practically satisfies the Maxwell equal area rule with a difference between the areas of approximately 9 %.

An example of microstructure that corresponds to the relaxed energy at external strain taken within the non-ellipticity zone is shown in Fig. 8. Each point is a particle; the color denotes its energy. One can see grains formed by the variants "a" and "b" of the triangular lattice. The grains contain particles with minimal energy. They are energetically indistinguishable and can be referred to as twins. The particles with the higher energy form grain boundaries, point defects and dislocations where the excess energy is localized.

Thus, the experimental observations fully comply with the theoretical point of view according to which the obtained envelope of the energy profile may be a quasiconvex envelope that corresponds to the energy minimizing microstructures. Theoretically, the envelope curve could have been a tangent line to both energy minima in the case of stress-free twinning; and the deviation from the straight line may be caused by the accumulation of the energy produced by internal stresses. One can see that grain boundaries and various defects are sources of energy accumulations in the case under consideration. And finally, twins automatically satisfy the Maxwell rule [3].

We conclude the investigations of structural transformations in a triangular lattice by the considerations of two-phase microstructures which appear on the straining path connecting the stress-free triangular phase "a" and the stressed square phase "d" (dashed straight line in Fig. 4b). The relaxed energy is shown in Fig. 9 (the

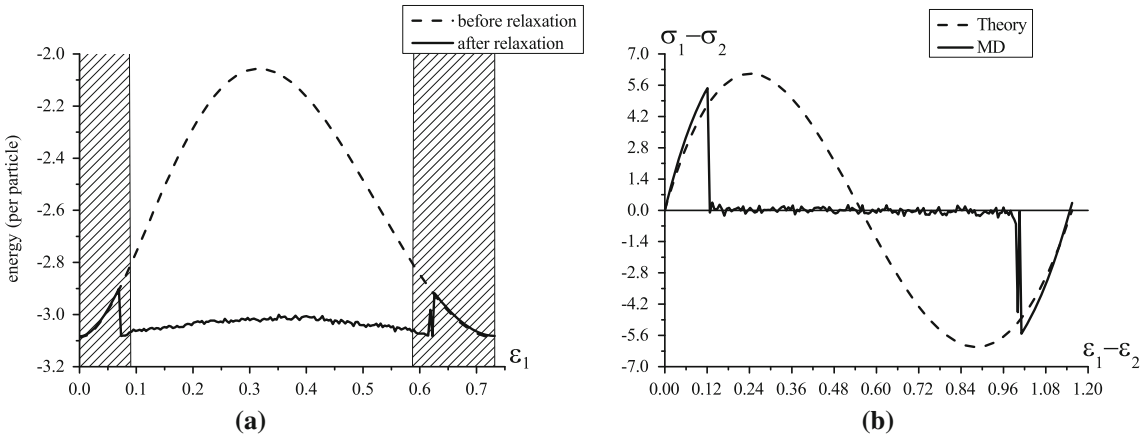

Fig. 7 Transition from triangular phase to triangular phase. Energy before (*dashed*) and after (*solid*) relaxation (**a**) and shear stress–shear strain diagram (**b**) along the constant volume straining path (*dash-dotted line* in Fig. 4a). Strong ellipticity zones are hatched. The Morse potential, $\theta = 6$

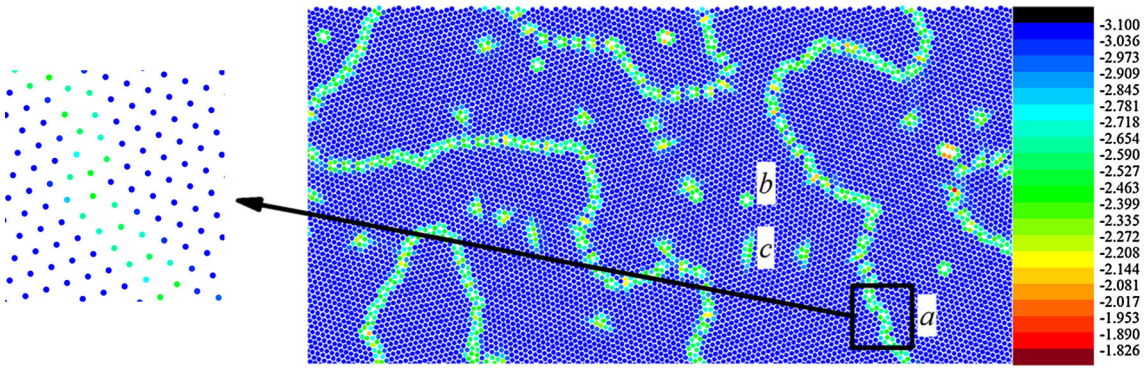

Fig. 8 Microstructures with grains formed by variants of triangular lattice within non-ellipticity zone at $\varepsilon_1 = 0.366$ (see Fig. 7). The Morse potential, $\theta = 6$. *a* Twins, *b* vacancies, *c* dislocations

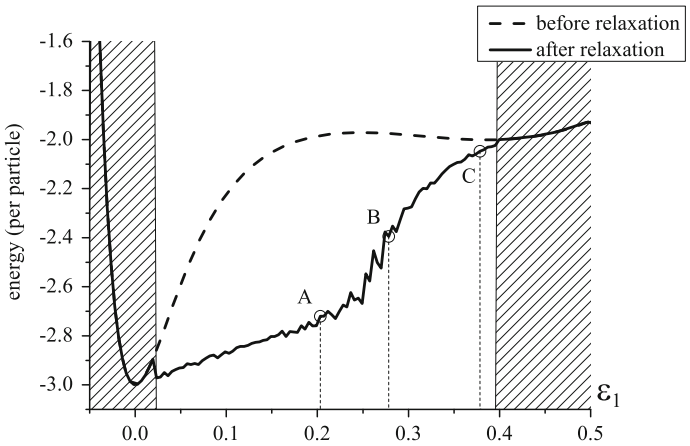

Fig. 9 Transition from triangular phase to square phase. Energy before (*dashed*) and after (*solid*) relaxation on *dashed line* shown in Fig. 4b. Strong ellipticity zones are hatched. The Morse potential, $\theta = 20$

dashed line reproduces the theoretical curve from Fig. 6a). The examples of microstructures corresponding to points A, B and C are shown in Figs. 10, 11 and 12, respectively.

Closer to the domain I, we see grains occupied by the triangle phase "a." In contrast to the constant volume path, more vacancies and microcracks appear at the straining path chosen here. The difference between Figs. 8

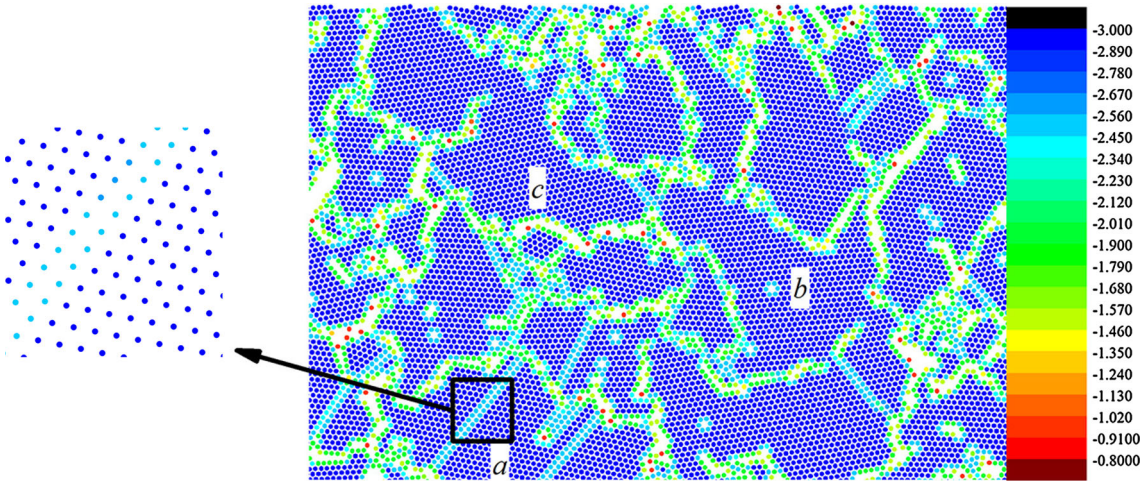

Fig. 10 Microstructures in non-ellipticity zone at strains "A" (see Fig. 9). The Morse potential, $\theta = 20$. *a* Triangular lattices divided by thin layers of square lattice, *b* vacancies, *c* microcracks

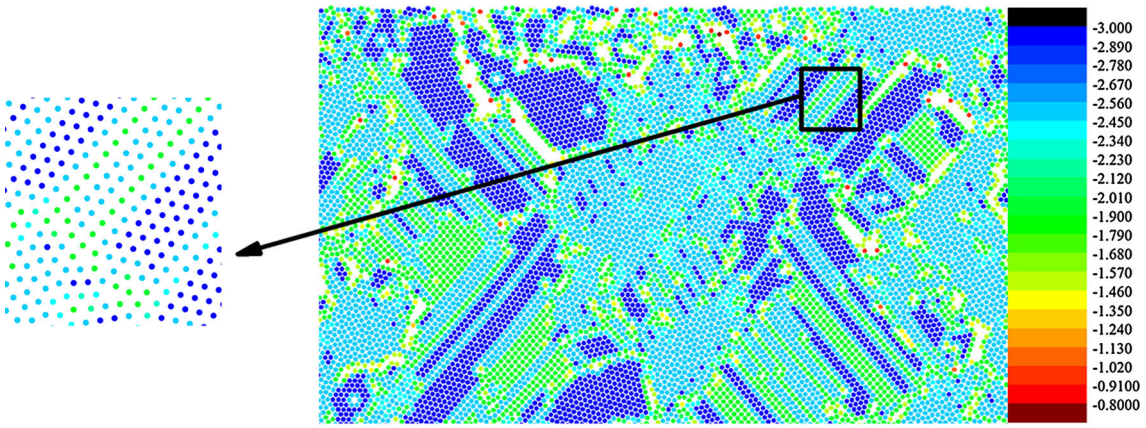

Fig. 11 Layered two-phase microstructure in non-ellipticity zone at strains "B" (see Fig. 9). The Morse potential, $\theta = 20$. Amorphous zones appeared

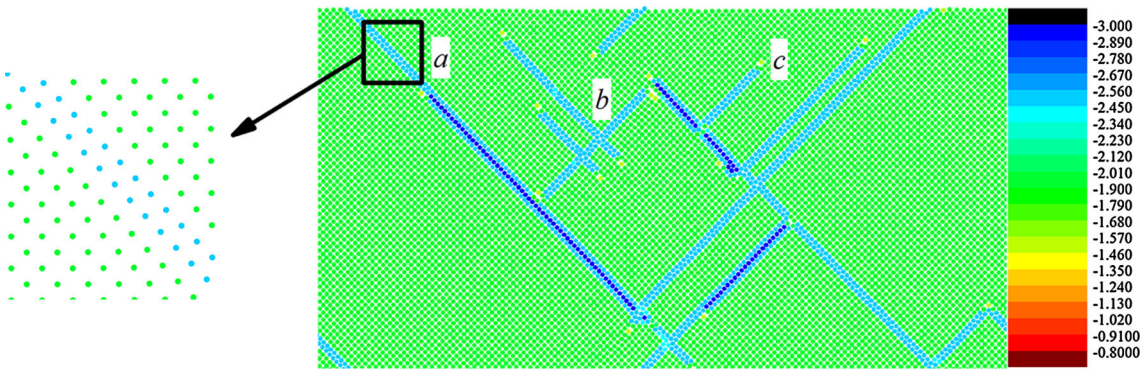

Fig. 12 Microstructures in non-ellipticity zone at strains "C" (see Fig. 9). The Morse potential, $\theta = 20$. *a* Domains of square lattices divided a shear band formed by a layer of triangular lattice, *b* a void formed at the cross section of two shear bands, *c* voids at the ends of shear bands

and 10 is that the grains are divided by thin layers of the square phase. As the external strain increases, a clearly marked layered two-phase microstructure develops. One can see in Fig. 11 that the supplied energy is distributed between coexisting domains occupied by low-energy variants of the triangular phase and high-

energy square phase. Finally almost all the material transforms into the square phase. In Fig. 12 one can also see shear bands formed by thin layers of the triangle phase and voids at the ends and intersections of shear bands. Note that the energy relaxation is connected not only with two-phase microstructures formation, but also with twinning, which is visible, although not specifically marked, in Fig. 10.

As in the case of twinning, these results comply with the general theoretical prediction [23] that two-phase microstructure nucleation and development is the mechanism of the energy relaxation in materials with non-convex energy.

5 Conclusions

Using both theoretical and MD experimental approaches, we studied structural transformations in a triangular lattice, as a general case of a planar simple lattice. The algorithm of strong ellipticity investigation is presented for the continuum, which is equivalent to a simple lattice in the sense of the Cauchy–Born energy and constructed within long-wave approximation. On the whole, five strong ellipticity domains in strain space were identified: three of them contain stress-free states of the triangular lattice variants, and the other two correspond to stressed square lattices. The size, the shape and the number of the domains depend on the interaction potential parameters. We showed that the energy profiles and stress-strain diagrams on the straining paths connecting the various strong ellipticity domains are typical for materials allowing twinning and martensite phase transformations. MD experiments supplemented the theoretical results by the "real" lattice behavior on the straining paths connecting the ellipticity domains. In fact, the energy envelope similar to the quasiconvex envelope corresponding to the energy minimizer was obtained experimentally for particular straining paths, and minimizing microstructures (twins, two-phase structures) were observed.

On the whole, we demonstrated the variety of behaviors of the lattice depending on straining paths and interaction potential parameters. We showed that the developed equivalent continuum approach and MD simulation together may be a proper instrument for bridging continuum and discrete mechanics of materials undergoing phase transformations.

Acknowledgments The authors are deeply grateful to the reviewers for their comments which have led to major improvements in the paper. This work was supported by Russian Foundation for Basic Research (Grant Nos. 12-01-31297 mol_a, 14-01-31487 mol_a, 13-01-00687).

Appendix

1. The Piola stress tensor is the transposed derivative of the energy (2) with respect to the deformation gradient [5],

$$\mathsf{P} = \left(\frac{\partial W}{\partial \mathsf{F}}\right)^{\mathrm{T}} = \frac{1}{2V_0}\sum_k \Pi'_k \frac{\partial a_k}{\partial \mathsf{F}^{\mathrm{T}}}.$$

We rewrite (1) as

$$\mathbf{a}_k = \mathsf{F}\cdot\mathbf{a}_k^0,$$

where

$$\mathbf{a}_k = a_k\mathbf{e}_k, \quad \mathbf{a}_k^0 = a_k^0\mathbf{e}_k^0, \qquad \not{\Sigma}.$$

Then the increment of the current bond length is

$$\delta a_k = \delta\sqrt{\mathbf{a}_k^0\mathbf{a}_k^0 \cdot\cdot\ (\mathsf{F}^{\mathrm{T}}\cdot\mathsf{F})} = \frac{1}{2a_k}\mathbf{a}_k^0\mathbf{a}_k^0 \cdot\cdot\ \delta\left(\mathsf{F}^{\mathrm{T}}\cdot\mathsf{F}\right) = \mathsf{F}\cdot\frac{\mathbf{a}_k^0\mathbf{a}_k^0}{a_k} \cdot\cdot\ \delta\mathsf{F}^{\mathrm{T}} = \frac{\mathbf{a}_k\mathbf{a}_k^0}{a_k} \cdot\cdot\ \delta\mathsf{F}^{\mathrm{T}}.$$

Thus,

$$\frac{\partial a_k}{\partial \mathsf{F}^{\mathrm{T}}} = \frac{\mathbf{a}_k^0\mathbf{a}_k}{a_k} = a_k^0\mathbf{e}_k^0\mathbf{e}_k,$$

and we arrive at formula (3):

$$\mathsf{P} = \frac{1}{2V_0}\sum_k \Pi'_k a_k^0 \mathbf{e}_k^0 \mathbf{e}_k.$$

We use the following notation for the tensor product of two vectors and the convolution of two tensors:

$$\mathbf{a}\otimes\mathbf{b} \equiv \mathbf{ab}, \qquad \mathbf{ab}\cdot\cdot\,\mathbf{cd} \equiv (\mathbf{b}\cdot\mathbf{c})\,(\mathbf{a}\cdot\mathbf{d}),$$

and the definition [5] of the derivative g'_{X} of the function g of tensor argument X that follows from the equality

$$\delta g\,(X_{kl}) = \frac{\partial g}{\partial X_{kl}}\delta X_{kl} = \frac{\partial g}{\partial X_{mn}}\mathbf{e}_m\mathbf{e}_n\cdot\cdot\,\mathbf{e}_l\mathbf{e}_k\delta X_{kl} = g'_{\mathsf{X}}\cdot\cdot\,\delta\mathsf{X}^{\mathrm{T}}.$$

The respective formula for the Cauchy stress tensor (4) is

$$\sigma = \frac{V_0}{V}\mathsf{F}\cdot\mathsf{P} = \frac{1}{2V}\sum_k \Pi'_k a_k \mathbf{e}_k\mathbf{e}_k.$$

2. To check the consistency, let us make sure that the equilibrium equations for simple lattices hold identically on both micro- and macroscopic levels following [18]. The microscopic equilibrium equation for any particle (which we can call reference particle, as the lattice is simple and infinite) has the form

$$\sum_k \mathbf{f}_k + \mathbf{b} = 0,$$

where $\mathbf{f}_k$ is the force with which the k th particle acts on the reference particle, and $\mathbf{b}$ corresponds to the external forces. It can be rewritten as

$$\frac{1}{2}\sum_k (\mathbf{f}_k + \mathbf{f}_{-k}) + \mathbf{b} = 0.$$

Let us assume that the forces depend only on $\mathbf{r}^0$, the reference position of the reference particle. Using long-wave approximation and taking Fig. 1a into account, we get

$$\mathbf{f}_{-k}\left(\mathbf{r}^0\right) = -\mathbf{f}_k\left(\mathbf{r}^0 - \mathbf{a}_k^0\right) \approx -\mathbf{f}_k\left(\mathbf{r}^0\right) + \mathbf{a}_k^0\cdot\overset{\circ}{\nabla}\mathbf{f}_k\left(\mathbf{r}^0\right).$$

Thus, the equilibrium equation yields

$$\overset{\circ}{\nabla}\cdot\frac{1}{2}\sum_k \mathbf{a}_k^0\mathbf{f}_k + \mathbf{b} = 0.$$

Introducing the body force

$$\mathbf{b}_{\mathrm{v}} = \frac{1}{V_0\rho_0}\mathbf{b},$$

we come to the continuum equilibrium equation

$$\overset{\circ}{\nabla}\cdot\mathsf{P} + \rho_0\mathbf{b}_{\mathrm{v}} = 0,$$

if the Piola stress tensor is

$$\mathsf{P} = \frac{1}{2V_0}\sum_k \mathbf{a}_k^0\mathbf{f}_k.$$

Due to the pair force interaction assumption

$$\mathbf{f}_k = \frac{\Pi'(a_k)}{a_k}\mathbf{a}_k,$$

and we once again arrive at formula (3) for the Piola stress tensor and thus demonstrate the equivalence of microscopic and continuum equilibrium equations.

3. Now let us turn to the equation of perturbed motion (5)

$$\rho_0 \delta \ddot{\mathbf{u}} = \delta \left(\overset{\circ}{\nabla} \cdot \mathsf{P} \right).$$

Denoting $\mathbf{v} = \delta \mathbf{u}$ and taking into account that $\overset{\circ}{\nabla}$ is written in the reference configuration, we get

$$\rho_0 \dot{\mathbf{v}} = \overset{\circ}{\nabla} \cdot \delta \mathsf{P}.$$

The Piola stress tensor depends on the deformation gradient only, so

$$\delta \mathsf{P} = \frac{\partial \mathsf{P}}{\partial \mathsf{F}^{\mathrm{T}}} \cdot\cdot \, \delta \mathsf{F}.$$

Let us calculate

$$\frac{\partial \mathsf{P}}{\partial \mathsf{F}^{\mathrm{T}}} = \frac{1}{2V_0} \sum_k \frac{\partial \Pi_k'}{\partial \mathsf{F}^{\mathrm{T}}} a_k^0 \mathbf{e}_k^0 \mathbf{e}_k + \frac{1}{2V_0} \sum_k \Pi_k' a_k^0 \mathbf{e}_k^0 \frac{\partial \mathbf{e}_k}{\partial \mathsf{F}^{\mathrm{T}}}.$$

Taking into account that

$$\delta \mathbf{e}_k = \delta \left(\frac{1}{a_k} \mathbf{a}_k \right) = -\frac{\mathbf{a}_k}{a_k^2} \frac{\mathbf{a}_k^0 \mathbf{a}_k}{a_k} \cdot\cdot \, \delta \mathsf{F} + \frac{1}{a_k} \mathsf{I} \mathbf{a}_k^0 \cdot\cdot \, \delta \mathsf{F}^{\mathrm{T}} = \frac{a_k^0}{a_k} \left(\sum_n \mathbf{i}_n \mathbf{e}_k^0 \mathbf{i}_n - \mathbf{e}_k \mathbf{e}_k^0 \mathbf{e}_k \right) \cdot\cdot \, \delta \mathsf{F}^{\mathrm{T}},$$

we get

$$\frac{\partial \mathbf{e}_k}{\partial \mathsf{F}^{\mathrm{T}}} = \frac{a_k^0}{a_k} \left(\sum_n \mathbf{i}_n \mathbf{e}_k^0 \mathbf{i}_n - \mathbf{e}_k \mathbf{e}_k^0 \mathbf{e}_k \right),$$

where unit tensor in the orthonormal basis $\mathbf{i}_n$ is

$$\mathsf{I} = \sum_n \mathbf{i}_n \mathbf{i}_n.$$

Thus,

$$\frac{\partial \mathsf{P}}{\partial \mathsf{F}^{\mathrm{T}}} = \frac{1}{2V_0} \sum_k \left[\frac{1}{a_k^2} \left(\Pi_k'' - \frac{\Pi_k'}{a_k} \right) \mathbf{a}_k^0 \mathbf{a}_k \mathbf{a}_k^0 \mathbf{a}_k + \sum_n \frac{\Pi_k'}{a_k} \mathbf{a}_k^0 \mathbf{i}_n \mathbf{a}_k^0 \mathbf{i}_n \right].$$

Since

$$\delta \mathsf{F} = \left(\overset{\circ}{\nabla} \delta \mathbf{r} \right)^{\mathrm{T}} = \left(\overset{\circ}{\nabla} \mathbf{v} \right)^{\mathrm{T}},$$

Eq. (5) yields

$$\delta \mathsf{P} = \frac{1}{2V_0} \sum_k \left[\frac{1}{a_k^2} \left(\Pi_k'' - \frac{\Pi_k'}{a_k} \right) \mathbf{a}_k^0 \mathbf{a}_k \mathbf{a}_k \mathbf{a}_k^0 + \frac{\Pi_k'}{a_k} \mathbf{a}_k^0 \mathsf{I} \mathbf{a}_k^0 \right] \cdot\cdot \, \overset{\circ}{\nabla} \mathbf{v}.$$

Taking into account that

$$\overset{\circ}{\nabla} = \left(\overset{\circ}{\nabla} \mathbf{r} \right) \cdot \nabla,$$

we get

$$\mathbf{a}_k^0 \cdot \overset{\circ}{\nabla} \mathbf{v} = \mathbf{a}_k \cdot \nabla \mathbf{v},$$

thus

$$\delta \mathsf{P} = \frac{1}{2V_0} \sum_k \left[\frac{1}{a_k^2} \left(\Pi_k'' - \frac{\Pi_k'}{a_k} \right) \mathbf{a}_k^0 \mathbf{a}_k \mathbf{a}_k \mathbf{a}_k \cdot\cdot \nabla \mathbf{v} + \frac{\Pi_k'}{a_k} \mathbf{a}_k^0 \mathbf{a}_k \cdot \nabla \mathbf{v} \right].$$

Finally,

$$\ddot{\mathbf{v}} = \frac{1}{\rho_0} \overset{\circ}{\nabla} \cdot \delta \mathsf{P} = {}^4\mathsf{Q} \cdot\cdot\cdot \nabla\nabla \mathbf{v},$$

where

$${}^4\mathsf{Q} = \left(\mathsf{I}\Phi + {}^4\Psi \right), \qquad \Phi = \frac{1}{2V_0\rho_0} \sum_k \frac{\Pi_k'}{a_k} \mathbf{a}_k \mathbf{a}_k,$$
$${}^4\Psi = \frac{1}{2V_0\rho_0} \sum_k \frac{1}{a_k^2} \left(\Pi_k'' - \frac{\Pi_k'}{a_k} \right) \mathbf{a}_k \mathbf{a}_k \mathbf{a}_k \mathbf{a}_k.$$

According to, e.g., [5], the strong ellipticity condition can be written in the following form:

$$\forall \mathbf{n}^0 \quad {}^4\mathsf{Q}^0 \cdot\cdot \mathbf{n}^0 \mathbf{n}^0 > 0, \quad Q^0_{ijkl} = \left(\frac{\partial^2 W}{\partial \left(\mathsf{F}^{\mathrm{T}} \right)^2} \right)_{jkil},$$

where

$${}^4\mathsf{Q}^0 = \left(\mathsf{I}\Phi^0 + {}^4\Psi^0 \right), \qquad \Phi^0 = \frac{1}{2V_0\rho_0} \sum_k \frac{\Pi_k'}{a_k} \mathbf{a}_k^0 \mathbf{a}_k^0,$$
$${}^4\Psi^0 = \frac{1}{2V_0\rho_0} \sum_k \frac{1}{a_k^2} \left(\Pi_k'' - \frac{\Pi_k'}{a_k} \right) \mathbf{a}_k \mathbf{a}_k \mathbf{a}_k^0 \mathbf{a}_k^0$$

and $\mathbf{n}^0$ indicates the direction of the wave vector in the reference configuration.
Taking into account that the unit vectors $\mathbf{n}^0$ in the reference and $\mathbf{n}$ in the current configuration are related as

$$\mathbf{n}^0 = \left(\mathbf{n} \cdot \mathsf{F} \cdot \mathsf{F}^{\mathrm{T}} \cdot \mathbf{n} \right)^{-1/2} \mathsf{F}^{\mathrm{T}} \cdot \mathbf{n}$$

and $\det(\mathsf{F}) > 0$, we get

$$\operatorname{sign}\left({}^4\mathsf{Q} \cdot\cdot \mathbf{n}\mathbf{n} \right) = \operatorname{sign}\left({}^4\mathsf{Q}^0 \cdot\cdot \mathbf{n}^0 \mathbf{n}^0 \right),$$

which means the equivalency of condition (7) and the conventional form of the strong ellipticity condition.

References

1. Grinfeld, M.A.: Thermodynamic Methods in the Theory of Heterogeneous Systems. Longman, New York (1991)
2. Silhavy, M.: The Mechanics and Thermodynamics of Continuous Media. Springer, Berlin (1997)
3. Gurtin, M.E.: Two-phase deformations of elastic solids. Arch. Rational Mech. Anal. **84**, 1–29 (1983)
4. Knowles, J.K., Sternberg, E.: On the failure of ellipticity and the emergence of discontinuous deformation gradients in plane finite elastostatics. J. Elasticity **8**, 329–379 (1978)
5. Lurie, A.I.: Nonlinear Theory of Elasticity. North-Holland, Amsterdam (1990)
6. Ogden, R.W.: Non-linear Elastic Deformations. Ellis Horwood, Chichester (1984)
7. Freidin, A.B., Chiskis, A.M.: Regions of phase transitions in nonlinear-elastic isotropic materials. Part 1: basic relations. Mech. Solids **29**(4), 91–109 (1994)
8. Freidin, A.B., Chiskis, A.M.: Regions of phase transitions in nonlinear-elastic isotropic materials. Part 2: incompressible materials with a potential depending on one of strain invariants. Mech. Solids **29**(4), 46–58 (1994)
9. Fu, Y.B., Freidin, A.B.: Characterization and stability of two-phase piecewise-homogeneous deformations. Proc. R. Soc. Lond. A **460**, 3065–3094 (2004)
10. Freidin, A.B., Fu, Y.B., Sharipova, L.L., Vilchevskaya, E.N.: Spherically symmetric two-phase deformations and phase transition zones. Int. J. Solids Struct. **43**, 4484–4508 (2006)
11. W, E., Ming, P.: Cauchy–Born rule and the stability of crystalline solids: static problems. Arch. Rational Mech. Anal. **183**(2), 241–297 (2007)

12. Hudson, T., Ortner, C.: On the stability of Bravais lattices and their Cauchy–Born approximations. ESAIM: M2AN **46**(1), 81–110 (2012)
13. Dobson, M., Luskin, M., Ortner, C.: Accuracy of quasicontinuum approximations near instabilities. J. Mech. Phys. Solids **58**(10), 1741–1757 (2010)
14. Born, M., Huang, K.: Dynamical Theory of Crystal Lattices. Clarendon, Oxford (1954)
15. Arroyo, M., Belytschko, T.: An atomistic-based finite deformation membrane for single layer crystalline films. J. Mech. Phys. Solids **50**(9), 1941–1977 (2002)
16. Sfyris, D., Sfyris, G., Galiotis, C.: Curvature dependent surface energy for a free standing monolayer graphene: some closed form solutions of the non-linear theory. Int. J. Nonlinear Mech. **67**, 186–197 (2014)
17. Ericksen, J.L.: On the Cauchy–Born rule. Math. Mech. Solids **13**(3-4), 199–220 (2008)
18. Krivtsov, A.M.: Deformation and Fracture of Solids with Microstructure. Fizmatlit, Moscow (2007) (**In Russian)**
19. Podolskaya, E.A., Panchenko, A.Yu., Krivtsov, A.M., Tkachev, P.V.: Stability of ideal infinite 2D crystal lattice. Doklady Phys. **57**(2), 92–95 (2012)
20. Verlet, L.: Computer "Experiments" on classical fluids. I. Thermodynamical properties of Lennard–Jones molecules. Phys. Rev. **159**, 98–103 (1967)
21. Krivtsov, A.M.: Energy oscillations in a one-dimensional crystal. Doklady Phys. **59**(9), 427–430 (2014)
22. Allen, M.P., Tildesley, D.J.: Computer Simulation of Liquids. Clarendon Press, Oxford (1987)
23. Ball, J.M., James, R.D.: Fine phase mixtures as minimizers of energy. Arch. Rational Mech. Anal. **100**, 13–52 (1987)